Submitted to the *Journal of Hydraulic Research*

Two-layer shallow water computation of mud flow intrusions into quiescent water

Su-Chin Chen [1,*], Szu-Hsien Peng [2] and Hervé Capart [3]

[1] Professor, Dept. of Soil and Water Conservation, National Chung-Hsing University, Taiwan, ROC.

[2] Ph.D. candidate, Dept. of Soil and Water Conservation, National Chung-Hsing University, Taiwan, ROC.

[3] Assistant professor, Dept. of Civil Engineering and Hydrotech Research Institute, National Taiwan University, Taiwan, ROC.

* Correspondence to:

Prof. Su-Chin Chen

Dept. of Soil and Water Conservation,

National Chung-Hsing University,

250 Kuo-Kuang Rd., Taichung 40227,

Taiwan, ROC

Telephone: +886-4-22851558

Fax: +886-4-22853967

e-mail: scchen@dragon.nchu.edu.tw

Abstract

The present computational study addresses two-layer shallow flows in which the superposed layers differ in velocity, density and rheology. The geomorphological phenomena motivating this model are confluence problems in which mud and debris surges slump into upland lakes and rivers. Specifically, the flows of interest are assumed to be sharply stratified, with a clear water layer flowing over a moving layer of mud modelled as a Herschel-Bulkley fluid. A finite volume computational scheme suitable for the simulation of such flows is presented and applied to various validation cases. The scheme extends to two-layer flows the robust method of Harten, Lax and Van Leer. Special care is devoted to the following numerical issues: the treatment of pressure along interfaces, the "contact points" at which the thickness of either layer can vanish, and the finite yield stress characterising the mud rheology. Results are presented for the intrusion of mud surges into shallow quiescent water.

Keywords: two-layer shallow water equations; Herschel-Bulkley fluid; confluence problem.

1 Introduction

The confluence of shallow currents having distinct compositions constitutes an important phenomenon in geomorphological hydraulics. Typical situations, widely encountered in upland Taiwan, involve the intrusion of mud flow or debris flow surges into lakes or rivers. The difference in composition between the tributary current and the receiving water body or stream has two important consequences. First, the density contrast may be large, with the sediment-laden inflow significantly heavier than the water it displaces. Secondly, the rheological properties of the intruding surge may differ greatly from those of water, with possible behaviours ranging from coarse-grained, stony inertial debris flow to fine-grained mud flow characterised by a plastic yield stress.

The intrusion of such currents into quiescent or flowing water may lead to significant hazards. Scenarios of practical concern include the transmission of surges across lake waters, and the possible partial or complete damming of river channels by tributary deposits. As an example, a series of such natural dam-formation events occurred in Taiwan following the Chichi earthquake of September 21, 1999, as documented in Chen (1999). Another example due to a typhoon flood is illustrated on Fig. 1. Confluence events and their consequences were analysed by Chen and Peng (2003a, 2003b) on the basis of field observations and laboratory experiments. In the present work, we seek to approach the issue using computational modelling.

A variety of modelling frameworks and computational schemes have been developed for both pure water shallow flows and single-layer currents characterised by special rheologies. A recent computational study of clear-water transients applied to 1D surges and dam-break waves was for example carried out by Hsu and Yeh (2002) using an explicit scheme. Jin and

Fread (1999) simulated 1D unsteady flows of mud/debris by including an additional friction slope term in the Saint-Venant momentum equation of their NWS FLDWAV model. A popular tool for hazard studies is the FLO-2D finite difference model of O'Brien et al. (1993), a horizontal two-dimensional code developed to simulate clear-water floods, mud flows and debris surges. The model can again be applied to either clear water or hyperconcentrated flow by tailoring the bottom resistance term. For mud flows, rheological descriptions which have been used include the Bingham fluid and the Herschel-Bulkley fluid models (Huang & Garcia, 1997, 1998; Imran et al., 2001).

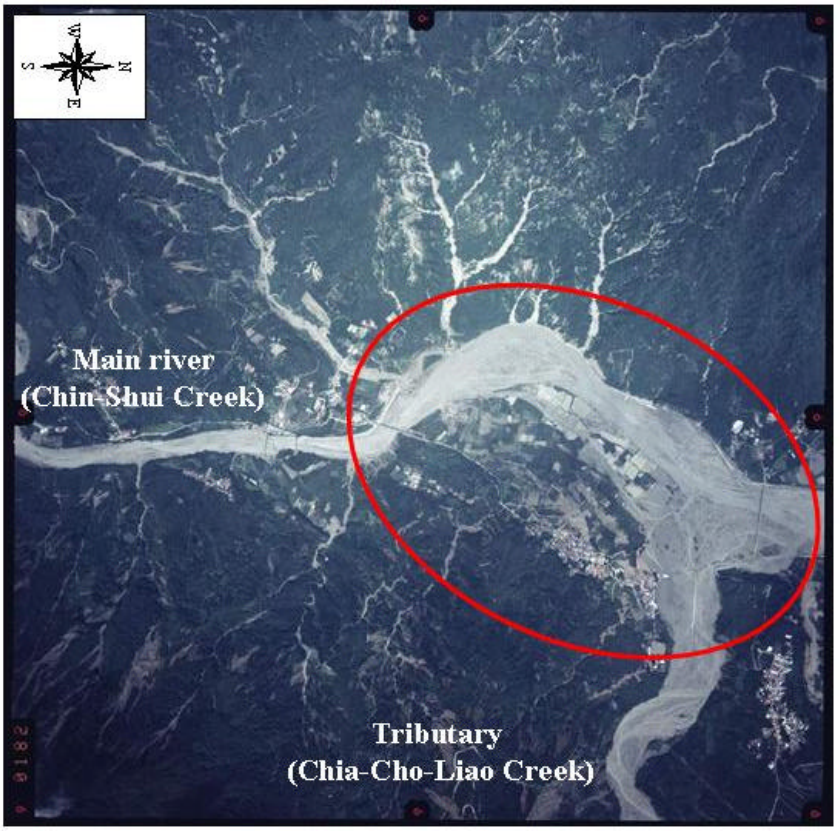

Figure 1. Aerial photograph of the debris flow deposit incurred at the confluence of Chia-Cho-Liao Creek and Chin-Shui River during Typhoon Toraji, September 2001, in Central Taiwan (Source: Fourth River Basin Management Bureau, WRA, Taiwan).

For the present purposes, a key limitation of the above models is that they postulate the flow of a single, effectively homogeneous layer everywhere in the domain of interest (even if the properties of this single layer are allowed to vary in time and space). For the present confluence problem, by contrast, the intruding surge and receiving water body are expected to retain their separate identities to a large extent. We therefore explore in the present work an alternative approach. Rather than instantaneously mix over their combined depth, we will assume that the incoming surge and receiving water superpose upon confluence into a sharply stratified two-layer flow (see Fig. 2). In addition to being endowed with distinct densities and velocities, as in classical two-layer shallow water flow (Abbott, 1979), the two layers will retain their separate rheological properties. Specifically, the behaviour of the lower layer will be described using the Herschel-Bulkley fluid model appropriate for mud flow. Interactions between the two layers will include both pressure and shear stresses along the interface, under the assumption that no mass transfer takes place.

While two-layer shallow water models are not nearly as mature as their single-layer counterparts, recent developments have been documented in Castro et al. (2001), Capart and Young (2002), Salmon (2002), and Montgomery and Moodie (2003). The scope of the present paper is restricted to first-order accurate computations of one-dimensional flows, but we address some specific numerical challenges associated with the confluence problem. These include the influence of the bottom topography, the special rheology of the lower layer (including the presence of a yield stress), and the occurrence of "contact points", or points where one of the two layers reaches zero thickness. As illustrated on Fig. 2b, such contact points may arise in three different ways for two-layer flows.

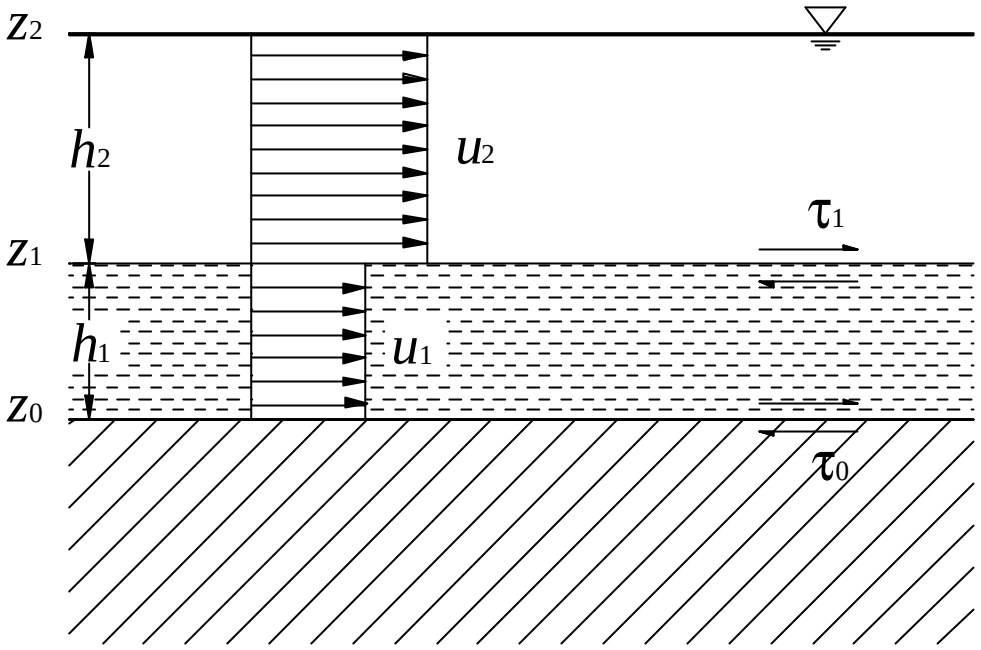

(a)

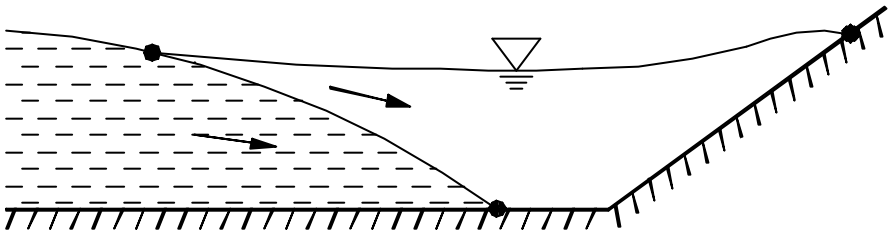

(b)

Figure 2. Idealised two-layer flow structure assumed in the present work: a) definition sketch; b) occurrence of "contact points" at locations where one of the layers reaches zero depth.

The present paper is organised as follows. Section 2 presents the governing equations and constitutive relations adopted. Section 3 details the computational scheme developed for two-layer flows with both density and rheology contrasts. Validation tests are presented in sections 4 and 5. The scheme is then applied in section 6 to two confluence cases, illustrating the phenomena which motivated the work. Finally section 7 draws some conclusions and

outlines perspectives for further research.

2 Governing equations

With reference to Fig. 2, the flows considered feature a shallow water layer on top of a shallow mud layer, in turn flowing over a rigid bottom. The two flowing layers are assumed to have distinct but constant densities r_1, r_2, with independent horizontal velocities u_1, u_2 taken to be uniform over the corresponding depths h_1 and h_2. Layer boundaries have elevations z_0, $z_1 = z_0 + h_1$ and $z_2 = z_0 + h_1 + h_2$, and are treated as sharp interfaces across which no mass transfer takes place. Momentum exchange occurs through shear stresses t_0 and t_1 applied along the interfaces and dependent upon the rheology of the shearing fluid.

Application of mass conservation and balance of momentum to the two layers yields the following governing equations (Abbott, 1979; Capart & Young, 2002):

$$\frac{\partial h_1}{\partial t} + \frac{\partial}{\partial x}(h_1 u_1) = 0, \tag{1}$$

$$\frac{\partial h_2}{\partial t} + \frac{\partial}{\partial x}(h_2 u_2) = 0, \tag{2}$$

$$\frac{\partial}{\partial t}(h_1 u_1) + \frac{\partial}{\partial x}(h_1 u_1^2 + \tfrac{1}{2} g h_1^2) + g h_1 \frac{\partial}{\partial x}\left(z_0 + \frac{r_2}{r_1} h_2 \right) = \frac{t_1 - t_0}{r_1}, \tag{3}$$

$$\frac{\partial}{\partial t}(h_2 u_2) + \frac{\partial}{\partial x}(h_2 u_2^2 + \tfrac{1}{2} g h_2^2) + g h_2 \frac{\partial}{\partial x}(z_0 + h_1) = -\frac{t_1}{r_2}, \tag{4}$$

where horizontal distance *x* and time *t* are the two independent variables, and where *g* is the gravitational acceleration. The usual hydrostatic pressure assumption is adopted throughout both layers and along the interfaces.

Because they remain valid when integrated across shocks, the momentum equations (3) and (4) will constitute the primary equations used in the present work. For certain purposes, however, it will also be useful to invoke the equations of motion

$$\frac{\partial u_1}{\partial t}+\frac{\partial}{\partial x}\left\{\frac{u_1^2}{2}+g\left(z_0+h_1+\frac{r_2}{r_1}h_2\right)\right\}=\frac{t_1-t_0}{r_1 h_1} \tag{5}$$

$$\frac{\partial u_2}{\partial t}+\frac{\partial}{\partial x}\left\{\frac{u_2^2}{2}+g(z_0+h_1+h_2)\right\}=-\frac{t_1}{r_2 h_2} \tag{6}$$

obtained upon expanding (3) and (4) by the chain rule and eliminating the depth evolution terms using the corresponding continuity equations. Two Bernoulli-type functions can be recognised inside the spatial derivatives. The above equations of motions are equivalent to the momentum equations for continuous, gradually varied flow, but their integration across discontinuities do not lead to physical shock relations.

Although the system of balance equations (1)-(4) is hyperbolic (Abbott, 1979), the four wave speeds l_1 to l_4 are not available in explicit closed form. Nevertheless, they can be bracketed within explicit bounds:

$$S_{\min} \le l_1 \le l_2 \le l_3 \le l_4 \le S_{\max}, \tag{7}$$

where $$S_{\min} = \min(u_1, u_2) - \sqrt{g(h_1+h_2)}, \tag{8}$$

and $$S_{\max} = \max(u_1, u_2) + \sqrt{g(h_1+h_2)}. \tag{9}$$

This is the only wave structure information which will be needed for the computations.

For each of the two interfaces z_1 and z_0, material on the upper side of the interface is assumed to be fluid-like and under shear, while material on the lower side of the interface is assumed solid-like and responding passively (through action = reaction) to the shear stress imposed on the upper side. The implied physical picture is that the mud behaves as a rigid

plug in the upper part of the mud layer, being under shear only at the base. As a consequence, the shear stress t_1 applied along interface z_1 is entirely ascribed to the turbulent water, while the shear stress t_0 along bottom z_0 is assumed to be fully controlled by the mud rheology. Accordingly, we represent shear stress t_1 using a Chézy-type formula

$$t_1 = r_1 C_f \, |u_2 - u_1| (u_2 - u_1), \tag{10}$$

where the only special feature is the scaling with velocity slip $u_2 - u_1$. Here the water velocity relative to the solid boundary is replaced by a velocity jump across the mud-water interface. For simplicity, the dimensionless friction coefficient C_f is taken to be constant, with a value to be calibrated or determined on the basis of empirical information.

To represent shear stress t_0 at the base of the mud layer, a more complicated rheology must be taken into account. Here the Herschel-Bulkley fluid model is adopted to describe the mud behaviour. A boundary layer argument is then needed to relate the vertical distribution of shear to the mean velocity of the mud layer, the thickness of the layer, and the bottom slope. Details about this approximation procedure and the Herschel-Bulkley rheological model are provided in Appendix A. The resulting basal shear stress t_0 is given by the expression

$$|t_0| = t_y + K \left[\frac{1 + \frac{1}{n}}{1 - \frac{nH}{(2n+1)h_1}} \right]^n \left(\frac{|u_1|}{H} \right)^n, \quad t_0 = |t_0| \frac{u_1}{|u_1|} \tag{11}$$

where t_y is the yield stress, K is a dynamic viscosity having dimensions $[ML^{-1}T^{n-2}]$, n is the flow index ranging between 0 and 1 for a shear-thinning fluid, $H = h_1 - t_y / (r_1 g \sin q)$ is the depth of the sheared zone, and $\sin q$ is the bottom slope. The depth H of the sheared zone is calculated as if the mud layer was flowing uniformly along an inclined plane subject only to the pull of its own weight.

To deal with regions where the mud layer is at rest, a condition for incipient motion must be provided. Following Liu and Huang (2002), we assume that motion occurs wherever the gravitational pull and stress gradient applied to the mud layer are sufficient to overcome the basal yield stress. In the present two-layer context, this threshold is obtained by setting velocity u_1 to zero in the equation of motion (5). Motion of the mud layer therefore occurs when

$$t_1 - r_1 g h_1 \frac{\partial}{\partial x}\left(z_0 + h_1 + \frac{r_2}{r_1} h_2 \right) > t_y . \qquad (12)$$

3. Computational scheme

The computational scheme adopted in the present work is an extension of the HLL scheme of Harten, Lax and Van Leer (1983), widely used for shallow single layer flows. Whereas the original HLL scheme applies to equations in full conservation form, the two-layer momentum equations feature non-conservative products associated with pressure along sloping interfaces. These terms are treated following the approach of Fraccarollo et al. (2003). Source terms associated with friction along the interfaces are further treated in point-implicit form.

In order to provide a reasonably compact presentation of the numerical scheme, it is useful to cast equations (1)-(4) in a more abstract form. First, the continuity equations (1) and (2) can both be written

$$\frac{\partial h_a}{\partial t} + \frac{\partial q_a}{\partial x} = 0 \qquad (13)$$

for $a = 1,2$, where the $q_a = h_a u_a$ denote flow rates. Likewise, the momentum equations (3) and (4) can both be cast in the form

$$\frac{\partial q_a}{\partial t} + \frac{\partial s_a}{\partial x} + g h_a \frac{\partial z_a}{\partial x} = s_a \tag{14}$$

where the $s_a = h_a u_a^2 + \frac{1}{2} g h_a^2$ are momentum fluxes, $z_1 = z_0 + r_2 / r_1 h_2$ and $z_2 = z_0 + h_1$ are hydrostatic pressure heads, and $s_1 = (t_1 - t_0)/r_1$ and $s_2 = -t_1 / r_2$ are momentum sources or sinks associated with the shear stresses.

The two continuity equations (13) are in full conservation form and can be integrated numerically using the explicit HLL scheme of Harten, Lax and Van Leer (1983). Dropping for conciseness the subscripts a, we need to discretise equations of the form

$$\frac{\partial h}{\partial t} + \frac{\partial q}{\partial x} = 0 . \tag{15}$$

Adopting a finite volume point-of-view, each depth $h(x)$ is discretised into piecewise constant segments h_i over finite intervals $x_{i-1/2} < x < x_{i+1/2}$ of constant length Δx. The corresponding discharges $q(x)$ are represented by fluxes $q_{i+1/2}$ sampled at the boundaries $x_{i+1/2}$ of the intervals. For each of the two equations (1) and (2), time stepping from time $t^{(k)}$ to time $t^{(k+1)} = t^{(k)} + \Delta t$ is achieved using the classical finite volume statement

$$h_i^{(k+1)} = h_i^{(k)} + \frac{\Delta t}{\Delta x}(q_{i-1/2}^{\mathrm{HLL}} - q_{i+1/2}^{\mathrm{HLL}}) \tag{16}$$

where
$$q_{i+1/2}^{\mathrm{HLL}} = \frac{S_{\mathrm{R}}}{S_{\mathrm{L}} - S_{\mathrm{R}}} q_i^{(k)} - \frac{S_{\mathrm{L}}}{S_{\mathrm{L}} - S_{\mathrm{R}}} q_{i+1}^{(k)} + \frac{S_{\mathrm{L}} S_{\mathrm{R}}}{S_{\mathrm{L}} - S_{\mathrm{R}}}(h_{i+1}^{(k)} - h_i^{(k)}) \tag{17}$$

is the standard HLL flux function. In the above formula, the left and right wave speeds S_{L} and S_{R} are estimated from

$$S_{\mathrm{L}} = \min(S_{\min,i}, S_{\min,i+1}, 0), \quad S_{\mathrm{R}} = \max(S_{\max,i}, S_{\max,i+1}, 0) \tag{18}$$

where $S_{\min}$ and $S_{\max}$ are the wave speed bounds given by expressions (8) and (9). Details about the HLL flux function and its conceptual basis can be found in Harten et al. (1983) and

Fraccarollo and Toro (1995).

The momentum equations taking the form (14) are more complicated to solve numerically because of the presence of non-conservative products $gh_a \partial z_a / \partial x$ and source terms s_a. We use Strang splitting (see e.g. Toro, 1999) to integrate these equations in two separate substeps. First, we use the LHLL scheme of Fraccarollo et al. (2003) to integrate the two equations

$$\frac{\partial q}{\partial t} + \frac{\partial s}{\partial x} + gh\frac{\partial z}{\partial x} = 0 \tag{19}$$

(again dropping the subscripts a) obtained by disregarding the source terms s_a.

The LHLL statement writes

$$q_i^{(k+1/2)} = q_i^{(k)} + \frac{\Delta t}{\Delta x}(s^{\mathrm{R}}_{i-1/2} - s^{\mathrm{L}}_{i+1/2}), \tag{20}$$

where

$$s^{\mathrm{L}}_{i+1/2} = s^{\mathrm{HLL}}_{i+1/2} - \frac{S_{\mathrm{L}}}{S_{\mathrm{R}} - S_{\mathrm{L}}}\frac{g(h_i^{(k)} + h_{i+1}^{(k)})}{2}(z^{(k)}_{i+1} - z^{(k)}_{i}) \tag{21}$$

and

$$s^{\mathrm{R}}_{i+1/2} = s^{\mathrm{HLL}}_{i+1/2} - \frac{S_{\mathrm{R}}}{S_{\mathrm{R}} - S_{\mathrm{L}}}\frac{g(h_i^{(k)} + h_{i+1}^{(k)})}{2}(z^{(k)}_{i+1} - z^{(k)}_{i}) \tag{22}$$

are lateralised corrections to the standard HLL flux

$$s^{\mathrm{HLL}}_{i+1/2} = \frac{S_{\mathrm{R}}}{S_{\mathrm{L}} - S_{\mathrm{R}}}s^{(k)}_{i} - \frac{S_{\mathrm{L}}}{S_{\mathrm{L}} - S_{\mathrm{R}}}s^{(k)}_{i+1} + \frac{S_{\mathrm{L}}S_{\mathrm{R}}}{S_{\mathrm{L}} - S_{\mathrm{R}}}(q^{(k)}_{i+1} - q^{(k)}_{i}). \tag{23}$$

In the above formulas, the wave speeds S_{L} and S_{R} are again estimated from eq. (18). The "lateralised flux correction" approach leading to the statements (20)-(22) is presented in Fraccarollo et al. (2003).

The second substep deals with the source terms by integrating the coupled pair of ODEs

$$\frac{\partial q_1}{\partial t} = s_1(q_1, q_2), \qquad \frac{\partial q_2}{\partial t} = s_2(q_1, q_2), \tag{24}$$

obtained by dropping the spatial derivatives from eq. (3) and (4) and assuming that $\partial h_1 / \partial t = \partial h_2 / \partial t = 0$. To guarantee unconditional stability, this integration is done in a point-implicit fashion. Using the implicit backward Euler scheme, we update the $q_a^{(k+1/2)}$ from fractional time level $k+1/2$ to the next time level $k+1$ according to statements

$$q_{1,i}^{(k+1)} = q_{1,i}^{(k+1/2)} + \Delta t\, s_1(q_{1,i}^{(k+1)}, q_{2,i}^{(k+1)}), \qquad q_{2,i}^{(k+1)} = q_{2,i}^{(k+1/2)} + \Delta t\, s_2(q_{1,i}^{(k+1)}, q_{2,i}^{(k+1)}). \tag{25}$$

Because of the relatively complicated shear stress function used in the present work (Herschel-Bulkley fluid), this pair of algebraic equations cannot be solved explicitly, and instead we use Newton's method to solve for the $q_a^{(k+1)}$ (see e.g. Gerald & Wheatley, 1999). Using the $q_a^{(k+1/2)}$ as initial values, convergence is obtained after a few iterations.

As the source terms are treated in a point-implicit fashion, the stability of the overall scheme depends on the HLL and LHLL steps used to update the $h_i^{(k+1)}$ and $q_i^{(k+1/2)}$. Since these updates are carried out using explicit statements, stability is subject to the Courant-Friedrichs-Levy (CFL) condition on the time step:

$$Cr = \frac{\Delta t}{\Delta x} l_{\max} \le 1, \tag{26}$$

where $l_{\max}$ is the maximum wave speed (in absolute value) over the computational domain, estimated from

$$l_{\max} = \max_i \{\max(|S_{\min,i}|, |S_{\max,i}|)\} \tag{27}$$

where $S_{\min}$ and $S_{\max}$ are again the wave speed bounds given by expressions (8) and (9). For the computations documented hereafter, Courant numbers in the range $Cr = 0.3$-0.9 are adopted.

One final difficulty that must be adressed by the numerical scheme is the possible occurrence of "contact points" (see Fig. 2b), where one of the layer depths h_a is finite at one location x_i but vanishes at the neighbouring location x_{i+1}. At such locations, fluxes $q_{a,i+1/2}$ and $s_{a,i+1/2}$ are treated using the above HLL and LHLL statements as long as the following condition is met

$$\frac{u_{a,i}^2}{2g} + h_{a,i} + z_{a,i} > z_{a-1,i+1}. \tag{28}$$

When the condition is not met, the section $x_{i+1/2}$ is treated as a solid wall where the flowing layer on the wet side of the contact point is entirely reflected. Condition (28) insures that reflection occurs only if the total head of the wetting front is insufficient to carry it past a local rise of the bottom interface.

We document below a series of tests conducted to validate the above numerical approach. Separate tests are first presented for flows involving a single water layer and a single mud layer, respectively. These are then complemented by simple tests involving two-layer flows.

4 Single layer model validation

4.1 Single water layer

To illustrate the behaviour of the standard HLL scheme, calculations for a single layer of water are first compared with the classical analytical solution of Stoker (1957) for the sudden breach of a dam over a horizontal frictionless bed. The initial data used by Wang and Shen (1999) are adopted: water depths to the left and right of the dam are set equal to 10 m and 1 m, respectively. The total length of the channel is 2000 m, the discretisation interval is $\Delta x = 2$ m, and the Courant number is set to $Cr = 0.9$. Results for different times t are plotted in

non-dimensional form on Fig. 3. It is checked that the numerical profiles converge towards the analytical solution as the ratio $t\sqrt{gh}/\Delta x$ grows, a longer time being equivalent to a finer discretisation. One significant advantage of the HLL scheme over other commonly used schemes (e.g. the Roe scheme) is that no specific fix is required at the transcritical transition, located for the dam-break example at position $x = 0$.

In order to further evaluate the model against measured data, we conducted small-scale dam-break tests in a laboratory flume. The experimental device is a plexiglas flume of length = 1 m, width = 0.1 m, and height = 0.15 m. The flume is fitted with a gate placed at a distance $x = 0.35\,\text{m}$ from the upstream end of the flume, and is closed both upstream and downstream in order to observe wave reflections. The evolving profiles of the dam-break waves are extracted from digital video sequences. For details regarding the experimental device and procedure, the reader is referred to Peng (2004). Two series of profiles are documented on Fig. 4, corresponding to distinct ratios of upstream to downstream depths. The bottom friction coefficient is set to $C_f = 0.01$ in both cases, and the discretisation interval is $\Delta x = 0.01$ m. Good correspondence is observed between the experimental and numerical results. In particular, the propagation of the bore and its reflection against the downstream wall are reasonably well-captured by the computations.

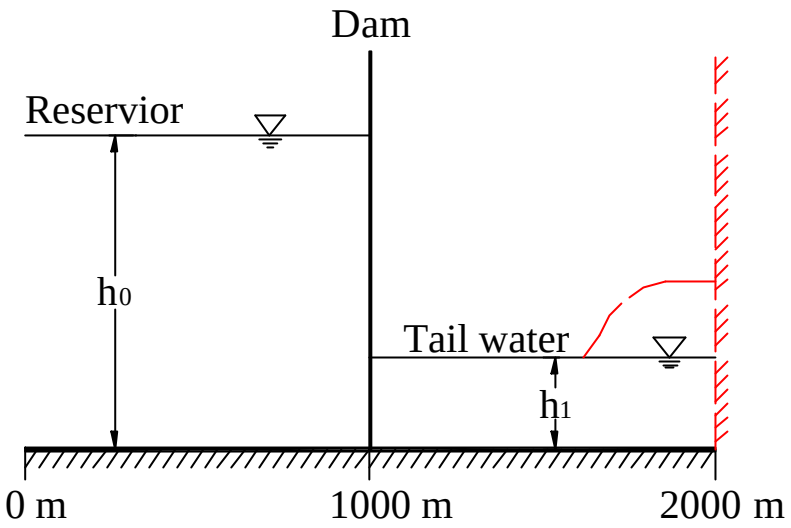

(a)

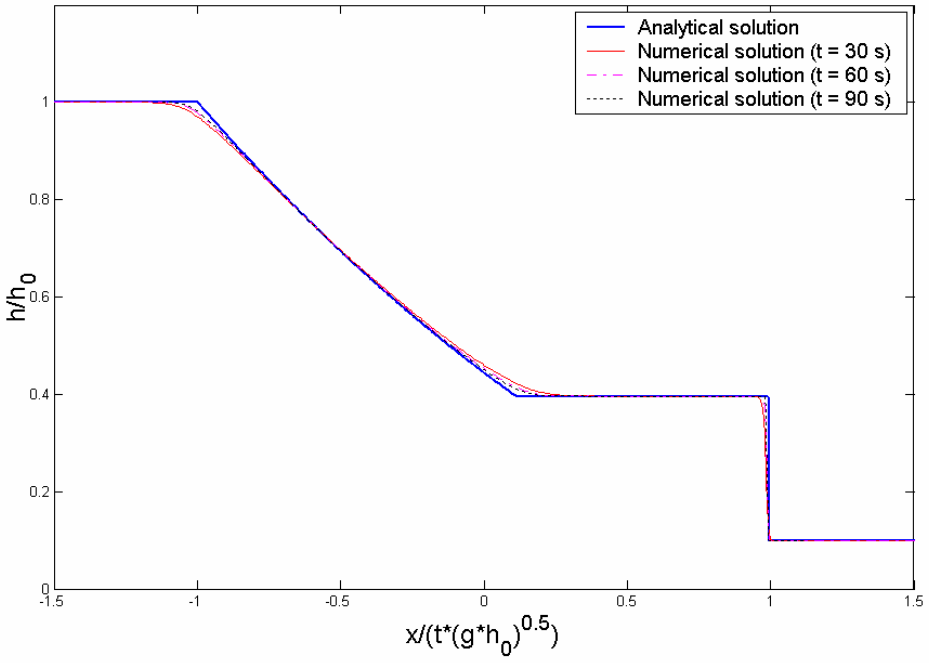

(b)

Figure 3. Comparison of analytical and numerical solutions for the flow of a single water layer: a) definition sketch; b) non-dimensional surface profiles.

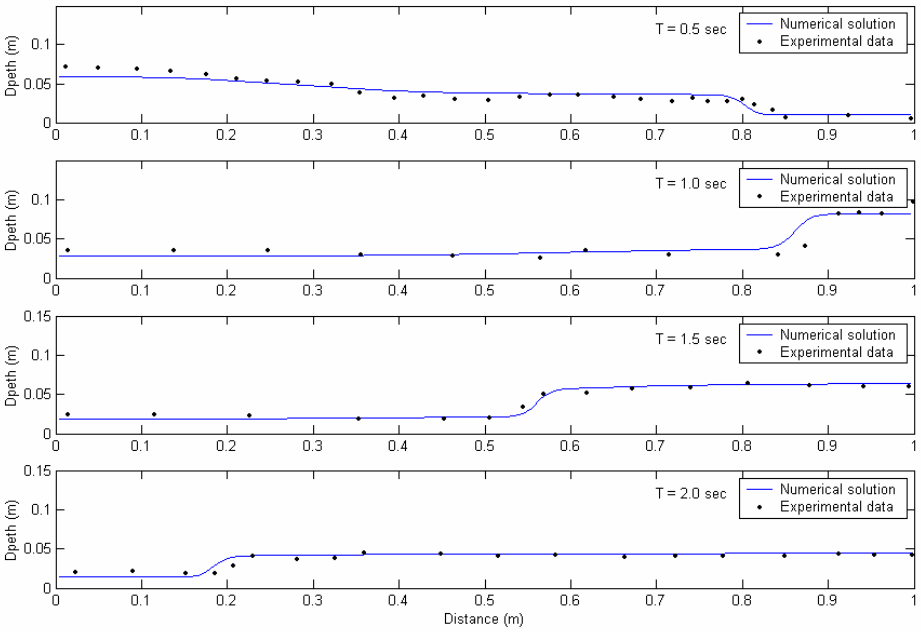

(a)

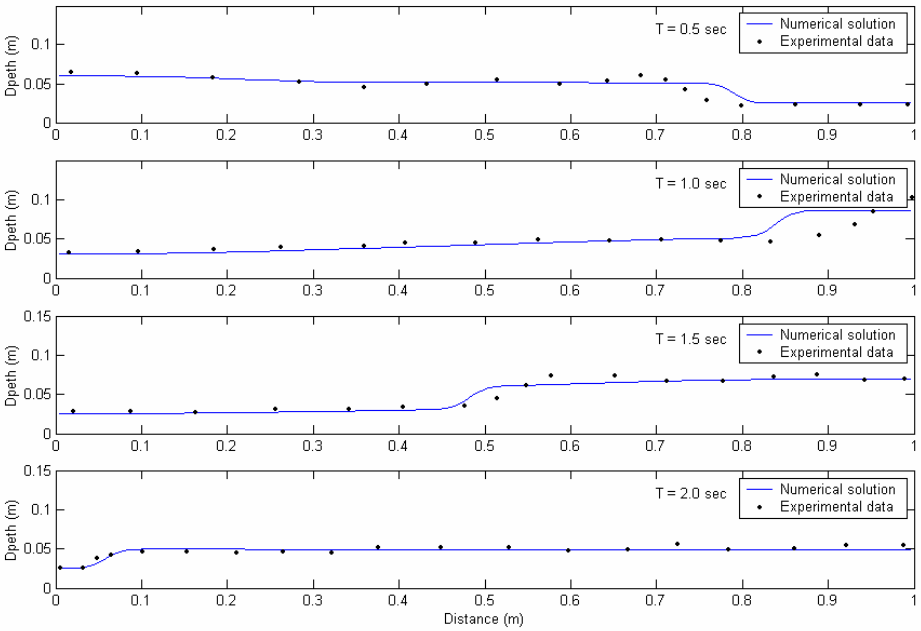

(b)

Figure 4. Comparison of numerical solutions and experimental data (Peng, 2004): a) upstream and downstream depths equal to 0.1 m and 0.01 m, respectively; b) upstream and downstream depths equal to 0.1 m and 0.03 m, respectively.

4.2 Single mud layer

To validate our treatment of the mud rheology, comparisons are sought with the experimental measurments of Liu and Mei (1989) for the flow of a mud surge down an inclined dry bed. The experiments were performed in a Plexiglas flume having length = 3.32 m, width = 0.076 m and height = 0.152 m. Inflow of kaolinite mixed with tap water was controlled by a gate at the upstream end of the flume. Mud flow profiles were recorded using a video camera 1.60 m downstream of the gate.

Two experimental runs are selected for comparison with numerical results. They are both obtained for the same mud composition, having density equal to 1,106 kg/m^3, but correspond to different flume slopes and inflow rates. The mud rheology is represented by the following Herschel-Bulkley parameters: yield stress $t_y = 0.875\,\mathrm{N/m^2}$, dynamic viscosity $K = 0.034\,\mathrm{Ns/m^2}$, and flow index $n = 1$ corresponding to a Bingham fluid (see Appendix A). Other experimental data are as follows for case 1: channel slope = 0.0257, phase speed = 5.22 cm/s, maximum depth = 0.71 cm, plug-flow depth = 0.31 cm; for case 2: channel slope = 0.0157, phase speed = 9.46 cm/s, maximum depth = 1.22 cm, plug-flow depth = 0.51 cm.

Computations are carried out for a single mud layer (water layer depth = 0), flowing as an unsteady surge over a dry sloping bed and subject to a constant discharge upstream. The numerical parameters are $\Delta x = 0.01\,\mathrm{m}$ and $Cr = 0.5$. Snapshots of the profiles are recorded once a steadily advancing surge is obtained. The results for case 1 and 2 are plotted on Fig. 5 against the measured data of Liu and Mei (1989). A reasonable correspondance is observed, providing some confidence in the present treatment of mud layer flow.

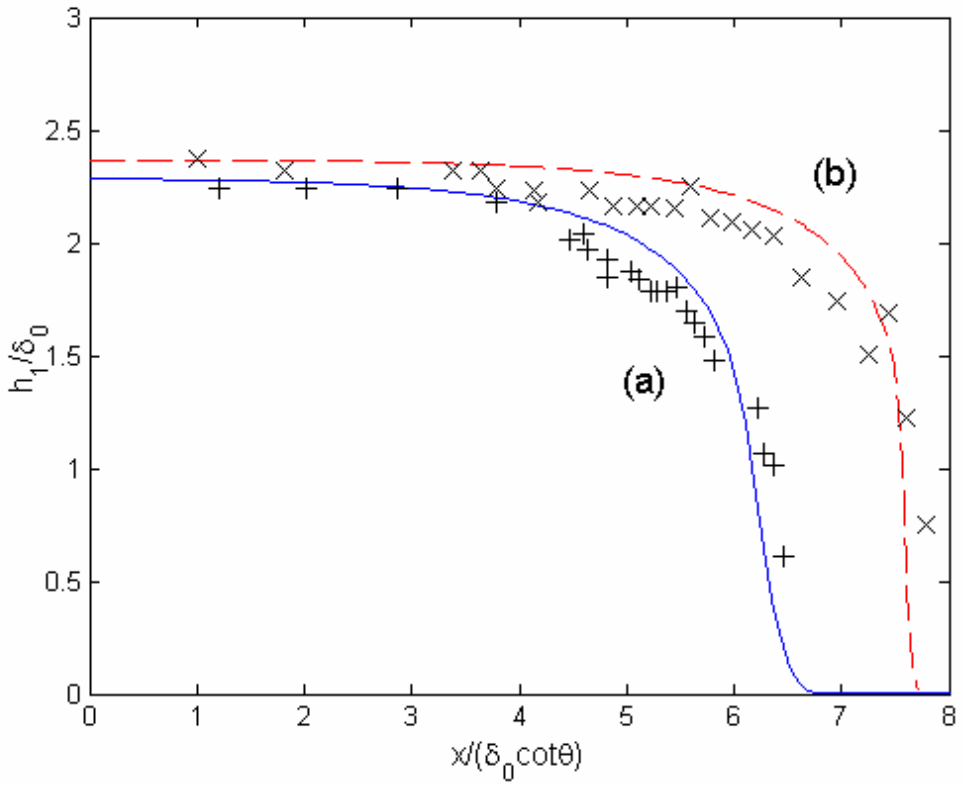

Figure 5. Comparison of numerical solutions with the experimental data of Liu and Mei (1989) for the flow of a mud surge down a dry incline: (+) measured surface profile for case 1; (×) measured profile for case 2; solid and dashed lines denote the computed profiles.

5 Two-layer model validation

5.1 Superposed layers of identical density

Owing to the increase in complexity, there are currently no known analytical benchmarks for transient two-layer flows with density contrasts $r_1 \neq r_2$. For the special case of a dam-break wave involving two layers of identical densities $r_1 = r_2$, however, the Stoker solution can be extended in a simple way. To see this, it is useful to subtract equation (5) from equation (6) to obtain

$$\frac{\partial(u_2 - u_1)}{\partial t} + \frac{\partial}{\partial x}\left\{\frac{u_1 + u_2}{2}(u_2 - u_1) + g\frac{r_1 - r_2}{r_1}h_2\right\} = 0 \qquad (29)$$

where the shear stresses t_0 and t_1 have been neglected. It is clear that if $r_1 = r_2$, the equation reduces to an advection equation for the velocity difference $u_2 - u_1$. This difference further stays equal to zero if it is uniformly set to zero at some initial time. Accordingly, if one sets $r_1 = r_2$, $u_1 = u_2 = u$, and $h = h_1 + h_2$ under the assumption that $t_0 = t_1 = 0$, and $\partial z_0 / \partial x = 0$, the set of equations (1)-(4) reduces to the three equations

$$\frac{\partial h}{\partial t} + \frac{\partial}{\partial x}(hu) = 0, \tag{30}$$

$$\frac{\partial}{\partial t}(hu) + \frac{\partial}{\partial x}(hu^2 + \tfrac{1}{2} g h^2) = 0, \tag{31}$$

$$\frac{\partial}{\partial t}\left(\frac{h_1}{h}\right) + u \frac{\partial}{\partial x}\left(\frac{h_1}{h}\right) = 0. \tag{32}$$

One recognises the continuity and momentum equations for a single layer complemented by a transport equation for the ratio $n = h_1 / h$. This ratio behaves like a passive tracer concentration advected with the fluid.

The Stoker solution can be extended in that case (see Leveque, 2002). Consider a Riemann initial value problem with variables h, u and $n = h_1 / h$ uniform on both sides of a discontinuity at location $x = 0$. The dambreak problem is obtained when $u = 0$ on both sides. The dambreak solutions for *h* and *u* are unchanged and correspond to the Stoker profiles, featuring the usual upstream rarefaction wave and downstream travelling bore. A third wave associated with eq. (32) takes the form of a contact discontinuity traveling at speed u. The ratios $n = h_1 / h$ are uniform on the left and right sides of the traveling discontinuity, keeping the constant values set by the initial conditions. This wave structure and the corresponding exact solution are illustrated on Fig. 6, for a case where the depth of the lower layer is the same on both sides of the dam and the depth of the upper layer is equal to zero downstream.

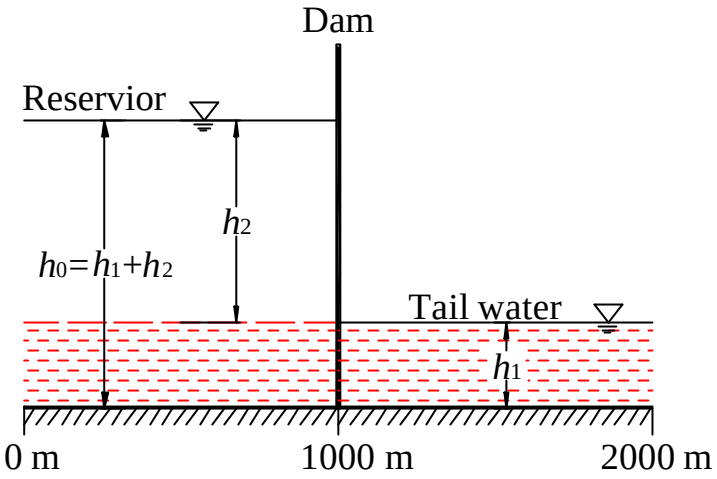

(a)

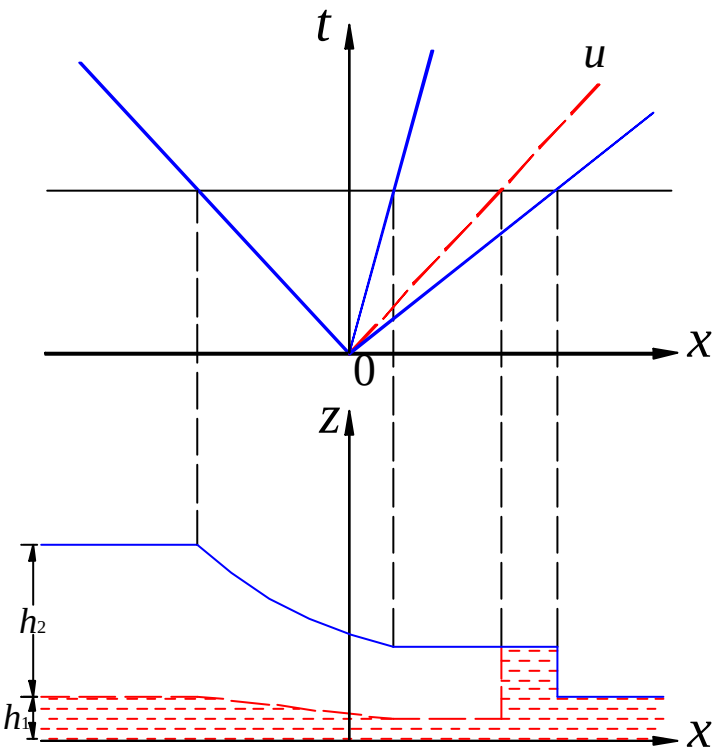

(b)

Figure 6. Dam-break flow involving two layers of equal densities $r_1 = r_2$: a) definition sketch; b) wave structure and exact solution.

Computational results for this special two-layer flow are compared with analytical profiles on Fig. 7a. As expected for a first order accurate scheme, the contact discontinuity in the central region of the flow is significantly smeared due to numerical diffusion. A more severe flaw of the model is observed downstream: a spurious fast wave of upper layer fluid is observed to propagate ahead of the bore. The generation of this spurious wave implies that our four-degrees of freedom two-layer scheme does not entirely converge to the three-degrees of freedom exact solution expected when $r_1 = r_2$. Instead, an extra wave associated with the fourth degree of freedom ($u_2 \neq u_1$) is generated in the first instants following the dam-break, and survives thereafter.

This flaw could be fixed by developing our numerical scheme on the basis of a different set of equations: continuity equations for layer 1 and layer 2, balance of total momentum $r_1 h_1 u_1 + r_2 h_2 u_2$, and equation (29) for the velocity difference $u_2 - u_1$. However this would lead to a different drawback: speeds of internal bores would no longer be correctly captured when $r_1 \neq r_2$. As documented in the next subsection, the correct capture of internal bores constitutes an important advantage of our scheme, and one that we wish to preserve.

Fortunately, it turns out that there is a much simpler fix: make the interface between layers 1 and 2 slightly frictional instead of perfectly frictionless. Results are shown on Fig. 7b for an interfacial friction coefficient set equal to $C_f = 0.03$ (friction along the bottom remains equal to zero). Only a moderate amount of friction is observed to be sufficient for the spurious wave to effectively vanish, yielding good agreement between computations and analytical profiles. While this frictional fix is not entirely satisfying, it is accepted as a temporary band-aid pending further work. In the applications of section 6, we will focus on flows with friction and density contrasts for which the scheme performs well.

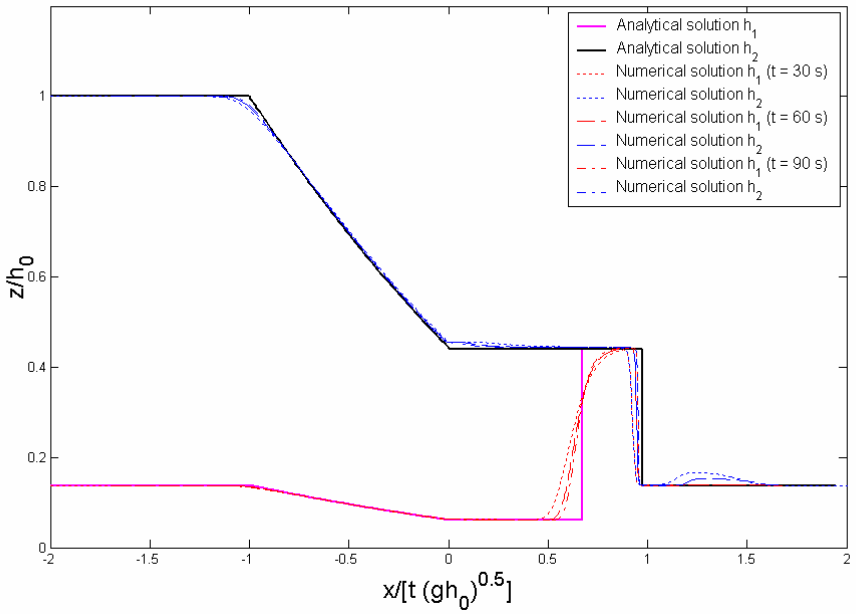

(a)

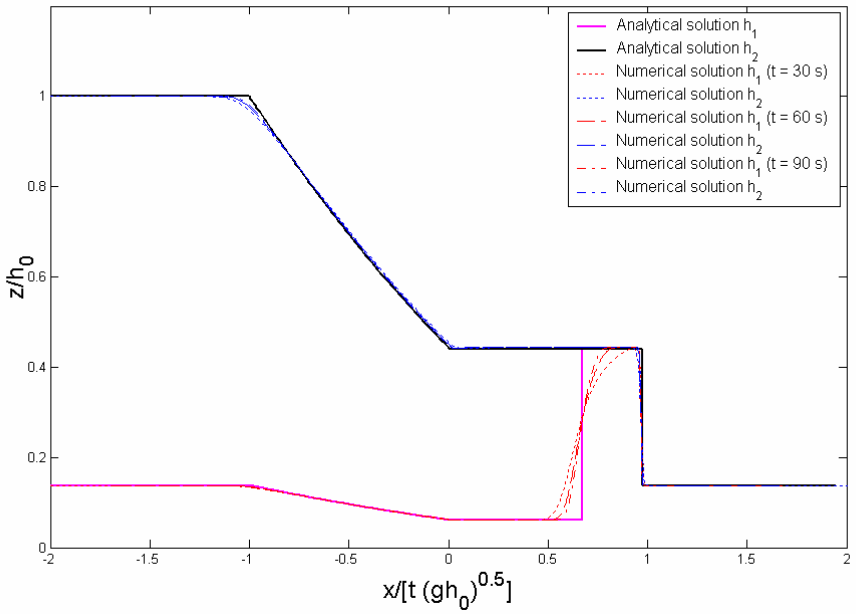

(b)

Figure 7. Comparison of numerical and analytical results for dam-break flow involving two layers of equal densities $r_1 = r_2$: a) two-layer numerical scheme without any friction; b) two-layer numerical scheme with moderate amount of friction between the two layers.

5.2 Internal hydraulic jumps

For two-layer flows with a finite density contrast $r_1 \neq r_2$, interesting exact solutions are associated with internal hydraulic jumps (Chien & Wan, 1991). Here again the shear stresses t_0 and t_1 are neglected. The simplest case, illustrated on Fig. 8a is one in which the bottom is horizontal, the upper layer is stationary ($u_2 = 0$), and the lower layer features a steady hydraulic jump. This internal hydraulic jump is similar in most respects to the hydraulic jumps of single layer flows: the only difference is that the upper layer exerts a hydrostatic pressure thrust on the jump interface. Absent any mass transfer between the two layers, equilibrium requires a horizontal free surface at the top of the stationary upper layer ($z_2 = z_0 + h_1 + h_2 = \text{const}$). Continuity is satisfied when the flow rate of the lower layer $q_1 = h_1 u_1$ is constant across the jump. Finally momentum balance of the lower layer is obtained when alternate depths h_1 and h_1' on both sides of the jump are related through

$$\frac{h_1'}{h_1} = \frac{1}{2}\left(\sqrt{1 + \hat{F}r_1^2} - 1\right), \tag{33}$$

where $\hat{F}r_1 = u_1 / \sqrt{\hat{g} h_1}$ is the upstream densimetric Froude number defined in terms of reduced gravity $\hat{g} = g(r_1 - r_2)/r_1$. To test the two-layer numerical scheme, a series of such flows was simulated by prescribing a stationary upper layer, supercritical lower layer depth h_1 and velocity u_1 upstream, and a constant discharge q and zero gradient $\partial h / \partial x$ downstream. Unsteady calculations subject to these conditions are found to converge to a steady state, yielding the profiles shown on Fig. 8b for two different cases. The treatment of the non-conservative pressure terms along the interface is found to successfully reproduce the expected horizontal free surface at the top of the upper layer.

Calculations for nine different cases with parameters in the range $\hat{F}r_1 = 1.85\sim9.40$ and $r_1 / r_2 = 1.1\sim1.7$ are further plotted on Fig. 8c against the theoretical relationship (33). Good agreement between numerical and analytical results is obtained, illustrating the advantages of the momentum-based formulation adopted for our numerical scheme. Formulations based on equation (29) instead of the two separate momentum equations (3)-(4) would not yield correct internal jumps, much as the momentum equation cannot be replace by the Bernoulli equation when modelling hydraulic jumps in single layer flows (see e.g. Abbott, 1979).

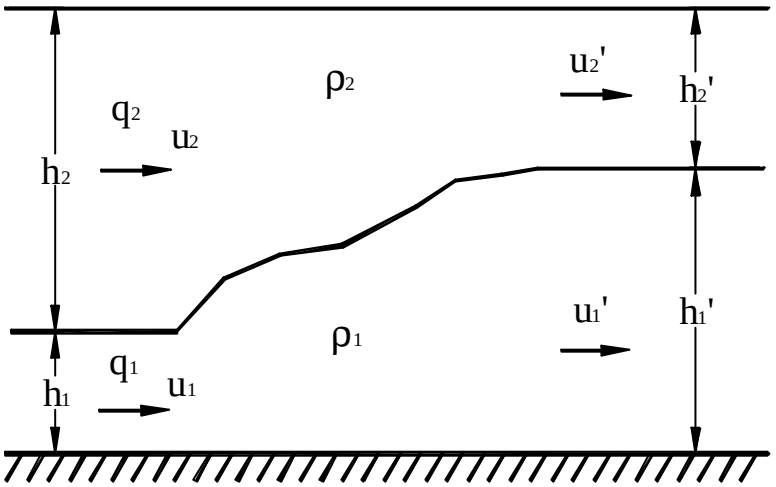

(a)

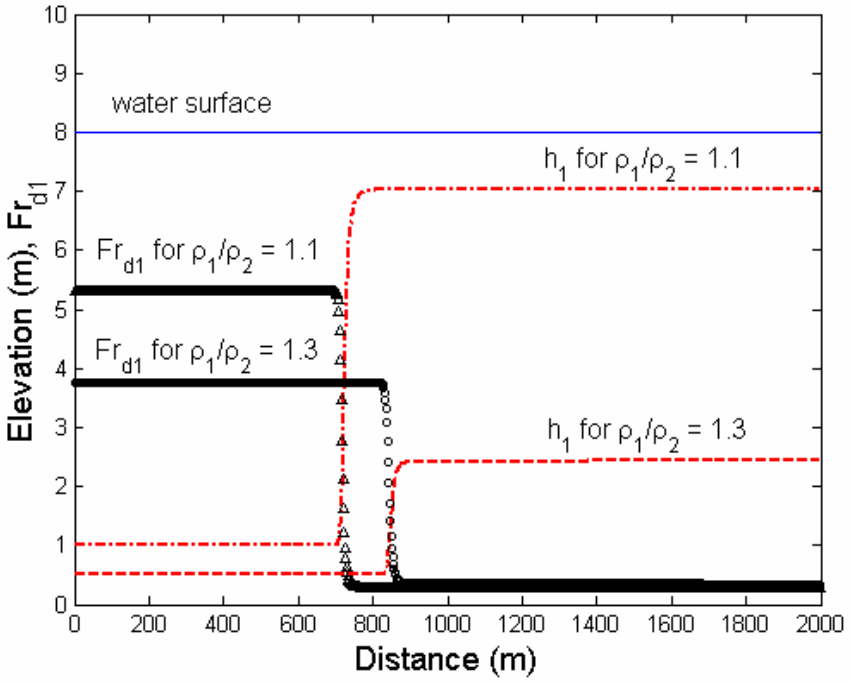

(b)

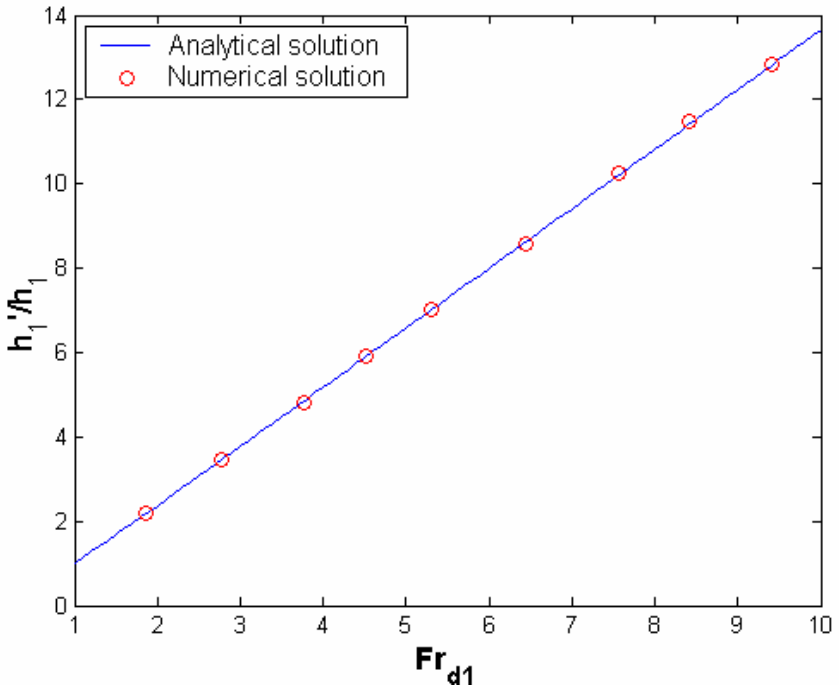

(c)

Figure 8. Internal hydraulic jump: a) definition sketch; b) calculated interface profiles for two examples; c) calculated ratios h_1'/h_1 (circles) compared with the theoretical relationship (line) for different values of the densimetric Froude number $\hat{F}r_1$.

6 Intrusion of mud surges into quiescent water

Having gained confidence in the numerical scheme, we can now devote our attention to the confluence applications which motivated the present work. The general problem considered is one in which a mudflow surge from a tributary invades a shallow river or lake. Since the present scheme is restricted to one horizontal dimension, the problem is examined only in a direction aligned with the tributary axis, and the water in the receiving body is assumed to be initially at rest. Such a situation is too idealised to represent an actual valley, but could be reproduced in a laboratory flume. Accordingly, the problem scales chosen for the simulations represent the typical dimensions of a small-scale laboratory device (like the flume used for the dam-break experiments of section 4.1). Likewise, the mud layer parameters are borrowed from the laboratory experiments of Liu and Mei (1989) used in section 4.2: density $r_1 = 1106$ kg/m^3, yield stress $t_y = 0.875$ N/m^2, dynamic viscosity $K = 0.034$ Ns/m^2, and flow index $n = 1$ corresponding to a Bingham fluid. The friction coefficient along the interface between the two layers is set equal to $C_f = 0.01$.

Two different configurations are examined. In both cases, the mud surge is initiated by a dambreak-type sudden release and flows down an incline of constant slope = 5 % into a channel of horizontal bottom. The two cases differ by the choice of geometry for the right bank of the channel. In the first case, a vertical wall is adopted as boundary condition, corresponding for instance to a dam face at one end of a reservoir. In the second case an adverse incline of constant slope = 10 % is adopted, corresponding to a sloping bank on the opposite side of a river. The initial conditions for the two different configurations are illustrated on Figures 9a and 11a.

Figure 9 shows a sequence of snapshots for the first case. As it invades the water body, the mud surge induces a bore propagating into the reservoir. The bore is reflected at the opposite vertical wall and interacts again with the mud flow intrusion as it hits back the left shore. Eventually, the flow motion decreases and the mud layer freezes into place due to its yield stress behaviour. A thin mud deposit is left along the upstream slope and a thick partially submerged deposit has accumulated downstream. The deposit features a characteristic break of slope at the new shoreline. While the mud and water layers started out as single layers separate from each other, the final state features superposed wedges with the displaced water overlying a static mud deposit. This type of dynamics could not be simulated without a two-layer approach allowing the lower and upper layers to adopt distinct velocities.

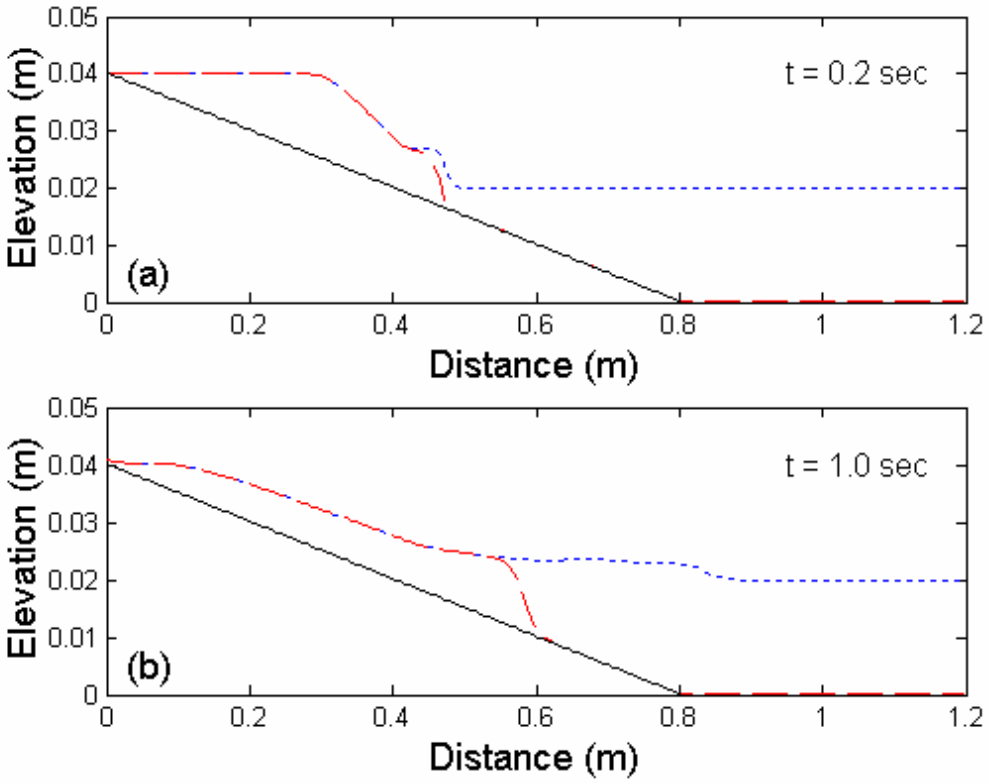

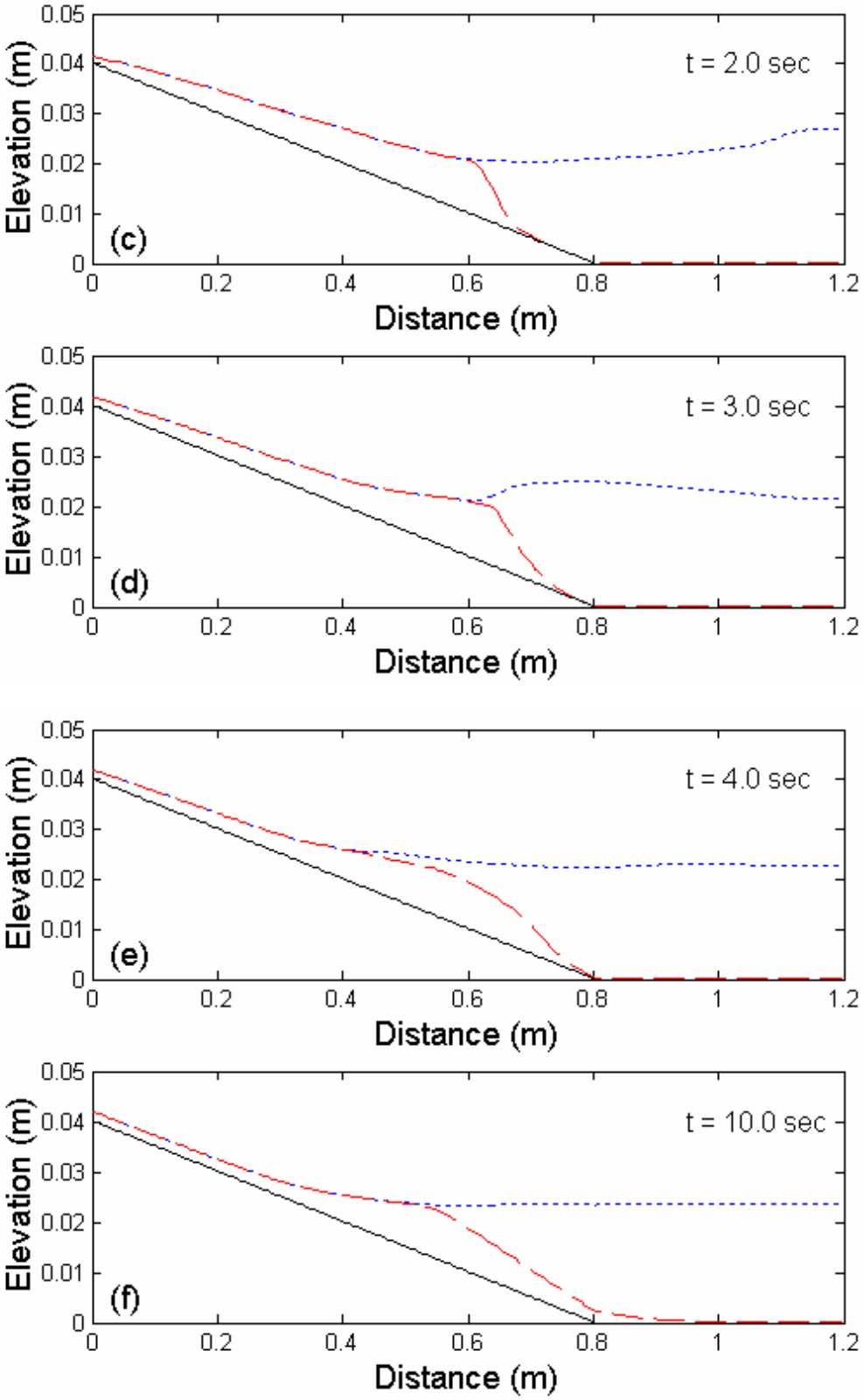

Figure 9. Simulation of mudflow intrusion into a shallow reservoir. On each snapshot of the sequence, the water surface is shown as a dotted line, the mud surface as a dashed line, and the underlying rigid bottom as a solid line.

The model can be used to examine the influence of the initial water level in the reservoir on the final shape of the mud deposit. Results for three simulations (all other conditions being the same as those of Fig. 9) are shown on Fig. 10. They were carried out for a zero water level (dry reservoir), an intermediate water level, and a high water level (the case detailed on Fig. 9). The results show a very significant influence of the water level. A higher water line causes the mild-sloped emerged deposit to accumulate further upstream, and prevents the steep-sloped submerged deposit from reaching very far into the reservoir. In the absence of water, the deposit accumulates at the toe of the tributary, featuring a smoothly curved mud profile that no longer exhibits a clear break of slope.

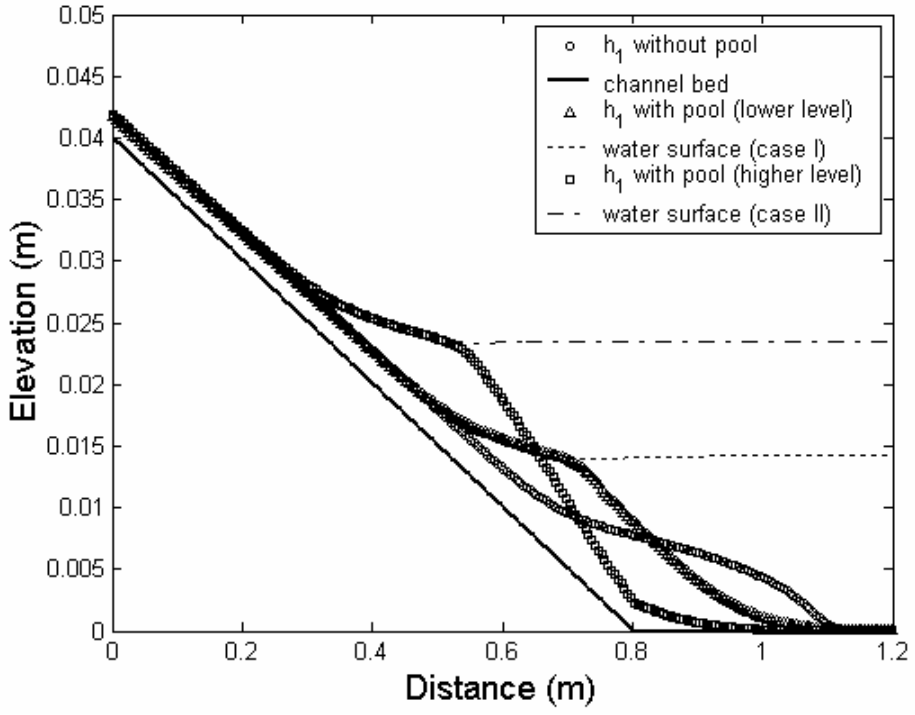

Figure 10. Mudflow intrusion into a shallow reservoir: final shape (t = 10 s) of the mud deposit for different initial water levels in the reservoir.

Figure 11 shows the sequence of snapshots obtained when the rigid wall of the first case (Fig. 9) is replaced by an adverse slope. Instead of being abruptly reflected, the water bore generated by the mudflow intrusion runs up the adverse slope before flowing back into the channel, exciting seiche oscillations that remain strong over a few periods and interact with the mudflow submergence. If the one-dimensional problem is taken to represent a transverse cut through a river channel fed by a tributary mudflow, it is clear that the mud deposit creates a significant partial obstruction of the channel. To model the interaction of the river current with the crossflow of mud, however, a horizontal two-dimensional treatment is needed. The results of Fig. 11 also underscore the importance of contact points, at which the thickness of one of the two layers vanishes. Such points occur at the edge of the bore run-up, at the tip of the submerged mud current, and at the shoreline break of slope. These various points play key roles in the overall dynamics, and remain well-behaved throughout the simulations.

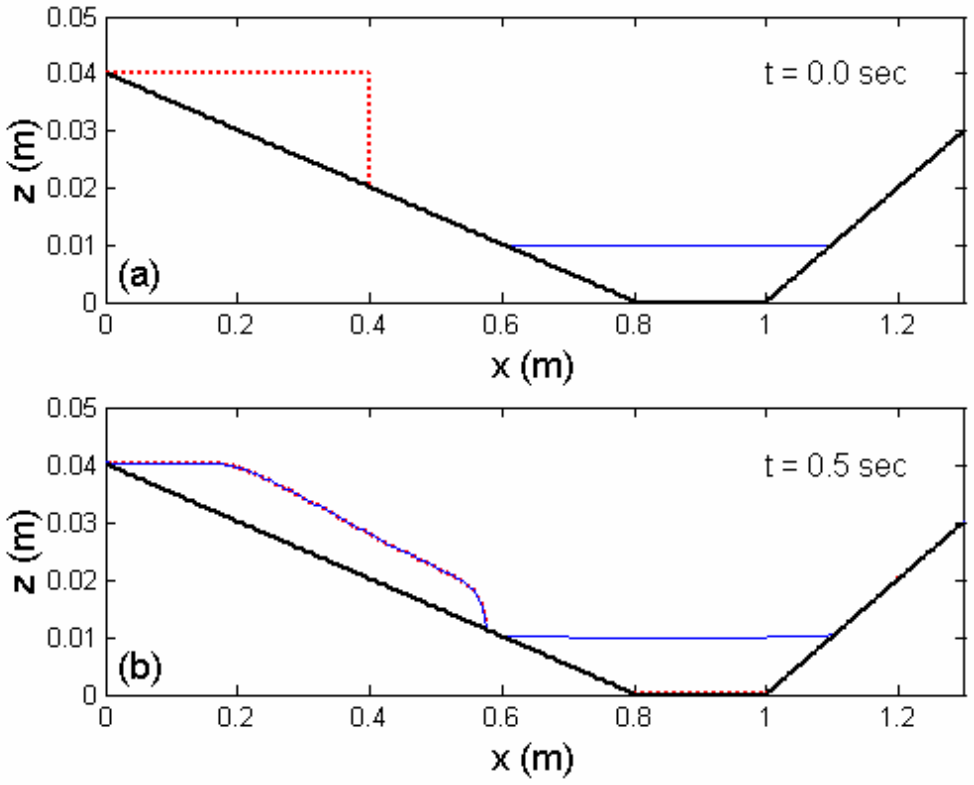

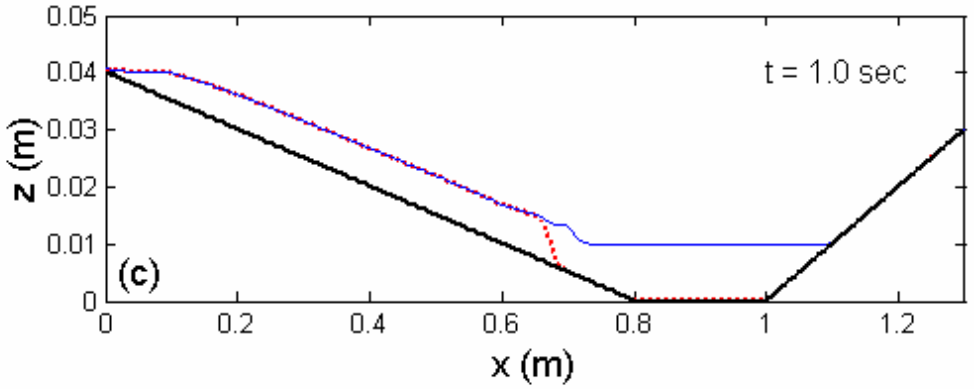
t = 1.0 sec
(c)
z (m)
x (m)
0.05
0.04
0.03
0.02
0.01
0
0.2
0.4
0.6
0.8
1
1.2

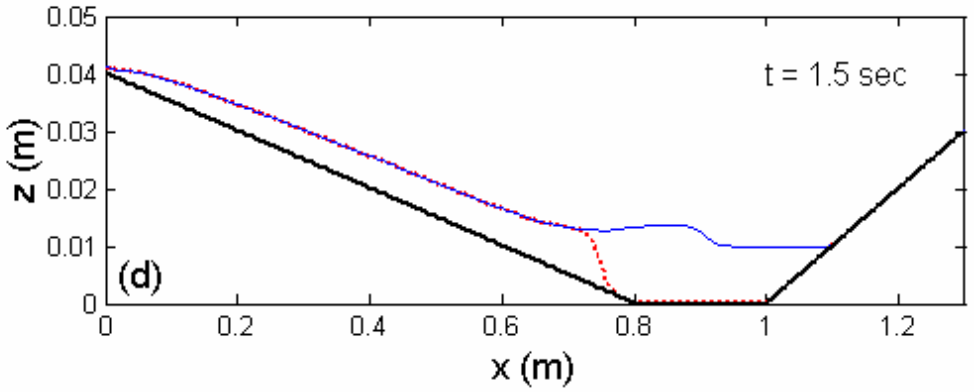
t = 1.5 sec
(d)
z (m)
x (m)
0.05
0.04
0.03
0.02
0.01
0
0.2
0.4
0.6
0.8
1
1.2

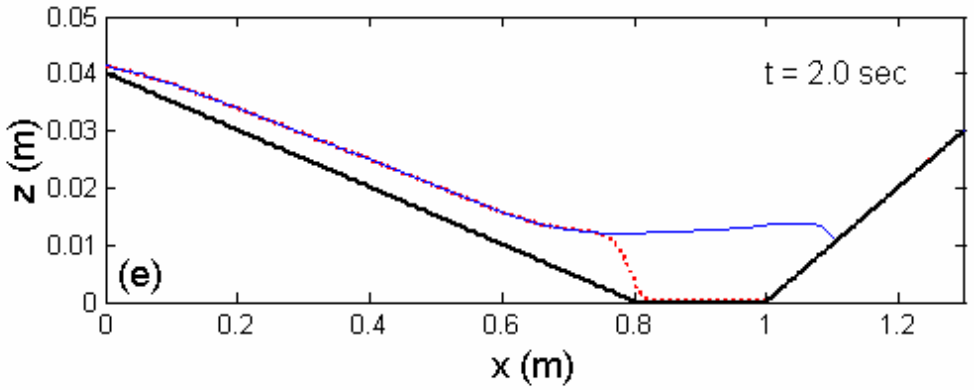
t = 2.0 sec
(e)
z (m)
x (m)
0.05
0.04
0.03
0.02
0.01
0
0.2
0.4
0.6
0.8
1
1.2

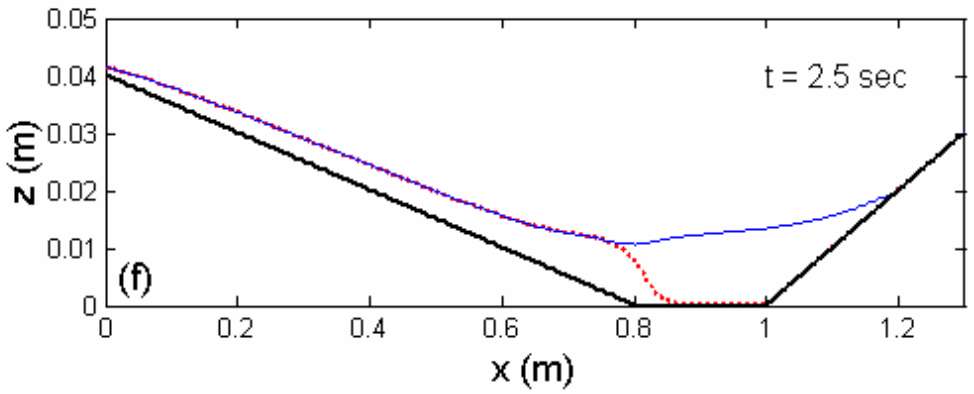
t = 2.5 sec
(f)
z (m)
x (m)
0.05
0.04
0.03
0.02
0.01
0
0.2
0.4
0.6
0.8
1
1.2

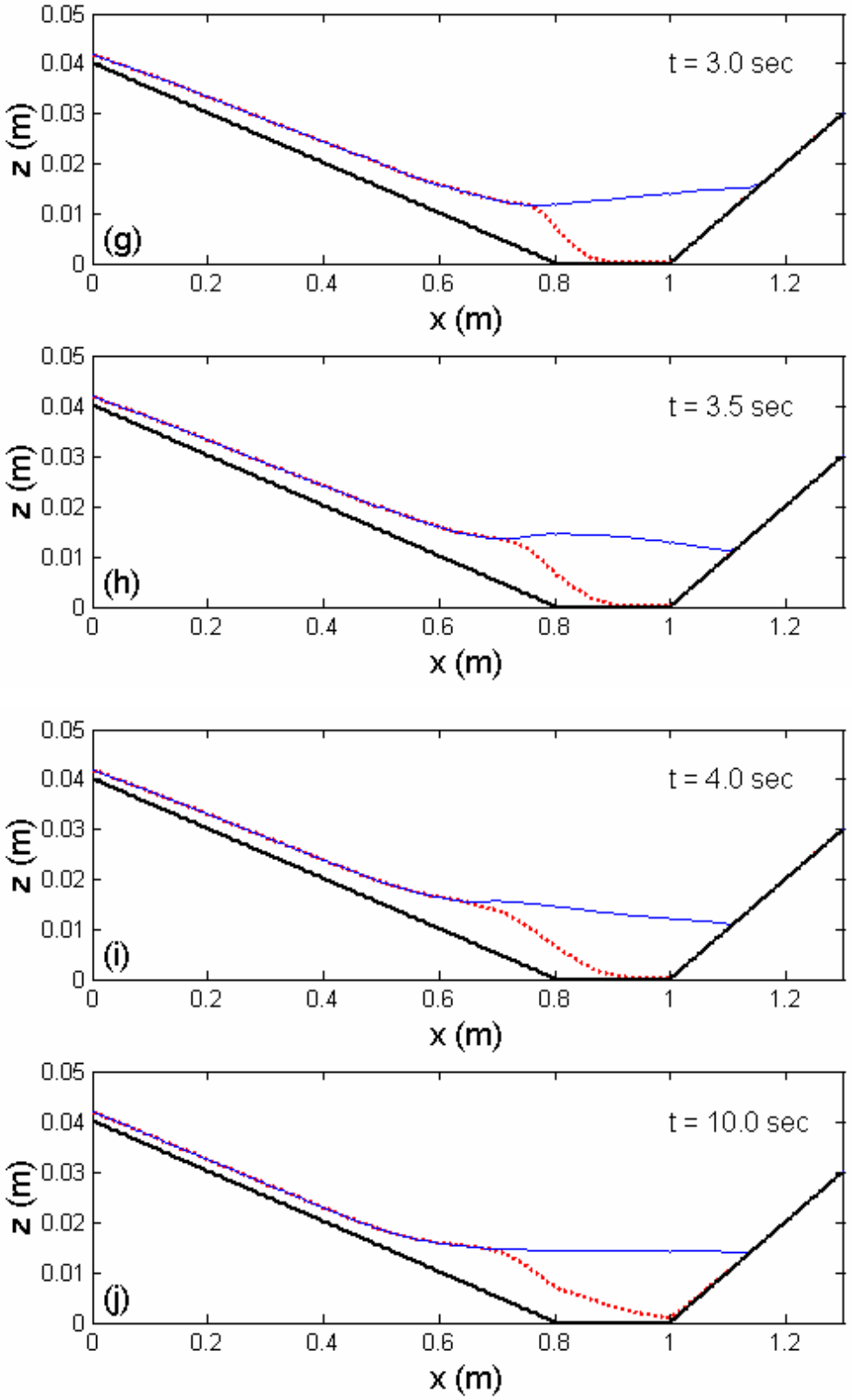

Figure 11. Simulation of mudflow intrusion into a river channel. On each snapshot of the sequence, the water surface is shown as a dotted line, the mud surface as a dashed line, and the underlying rigid bottom as a solid line.

7 Conclusions and perspectives

In the present work, a two-layer model was developed to describe the confluence of shallow currents having distinct compositions. Various numerical difficulties were discussed, including the treatment of non-conservative products, source terms, and contact points in two-layer computations. The solutions proposed to address these difficulties were found to perform satisfactorily for a number of single layer and two-layer validation cases. They were also found to be sufficiently robust to be applied to calculations of confluence events. The results obtained for mudflow intrusions into idealised reservoirs and channels provide insight into geomorphologically significant events, illustrating the potential of the two-layer approach. Features captured in the simulations include the generation of water bores and the formation of mud deposits with sharp breaks of slope at the shoreline.

Nevertheless, a number of challenges remain. From a numerical point of view, limitations of the present approach were manifested by the generation of a spurious wave in dam-break flows involving two frictionless layers of the same density. Extension to second order accuracy would also be desirable to better resolve fragile features such as weak shocks and contact discontinuities. From the point of view of geomorphological applications, a key step to be taken is to extend the present one-dimensional approach to horizontal two-dimensional flows. Field and laboratory observations indicate that valley topography and crossflow interactions exert a very significant influence on confluence events. Horizontal two-dimensional simulations could contribute to a better understanding of these effects, and work in this direction is currently in progress.

Acknowledgements

This research was supported by a grant from the National Science Council, R.O.C. (Project no. NSC 92-2313-B-005-093). In part of support for the participation of H. Capart in the present computational developments was provided by the National Science Council of the Republic of China under grant no. 92-2211-E-002-062.

References

1. Abbott, M.B. (1979), *Computational hydraulics: elements of the theory of free surface flows*, Pitman.
2. Capart, H. and D.L. Young (2002), "Two-layer shallow water computations of torrential geomorphic flows," In *Proceedings of the International Conference on Fluvial Hydraulics*, Bousmar & Zech (eds), pp. 1003-1012.
3. Castro, M., Macias, J. and C. Pares (2001), "A Q-scheme for a class of systems of coupled conservation laws with source term. Application to a two-layer 1-D shallow water system," *Math. Modell. and Numer. Anal.*, 35(1): 107-127.
4. Chen, S.C. (1999), "Failure mechanism and disaster mitigation on landslide-dammed lakes," *J. Chin. Soil Water Conserv.*, 30(4): 299-311. (in Chinese)
5. Chen, S.C. and S.H. Peng (2003a), "Confluence of debris slides and river flows in Taiwan," In *Proceedings of the International Conference on Slope Engineering*, Hongkong, China, pp. 757-762.
6. Chen, S.C. and S.H. Peng (2003b), "Experiment of confluence between main river and tributary by applying digital image processing," *J. Chin. Soil Water Conserv.*, 34(2): 195-205. (in Chinese)
7. Chien, N. and Z.H. Wan (1991), *Mechanics of sediment transport*, Science Press. (in Chinese)

8. Fraccarollo, L., and E.F. Toro (1995), "Experimental and numerical assessment of the shallow water model for two-dimensional dam-break type problems," *J. Hydr. Res.*, 33(6): 843-864.

9. Fraccarollo, L., Capart, H. and Y. Zech (2003), "A Godunov method for the computation of erosional shallow water transients," *Int. J. Numer. Meth. Fluids*, 41: 951-976.

10. Gerald, C.F. and P.O. Wheatley (1999), *Applied numerical analysis*, Addison Wesley Longman.

11. Harten, A., Lax, P.D. and B. van Leer (1983), "On upstream difference and Godunov-type schemes for hyperbolic conservation laws," *SIAM Review*, 25: 35-61.

12. Hsu, C.T. and K.C. Yeh (2002), "Iterative explicit simulation of 1D surges and dam-break flows," *Int. J. Numer. Meth. Fluids*, 38: 647-675.

13. Huang, X. and M.H. Garcia (1997), "A perturbation solution for Bingham-plastic mudflows," *J. Hydr. Engrg.*, ASCE, 123(11): 986-994.

14. Huang, X. and M.H. Garcia (1998), "A Herschel-Bulkley model for mud flow down a slope," *J. Fluid Mech.*, 374: 305-333.

15. Imran, J., Parker, G., Locat, J. and H. Lee (2001), "A 1-D numerical model of muddy subaqueous and subaerial debris flows," *J. Hydr. Engrg.*, ASCE, 127(11): 959-968.

16. Jin, M. and D.L. Fread (1999), "1D modeling of mud/debris unsteady flows," *J. of Hydraulic Engineering*, ASCE, 125(8): 827-834.

17. Leveque, R.J. (2002), *Finite Volume Methods for Hyperbolic Problems*, Cambridge Univ. Press.

18. Liu, K.F. and C.C. Mei (1989), "Slow spreading of a sheet of Bingham fluid on an inclined plane," *J. Fluid Mech.*, 207: 505-529.

19. Liu, K.F. and M.C. Huang (2002), "The numerical simulation of debris flows and its application in Shen-Mu Village," *J. Chin. Soil Water Conserv.*, 33(3): 215-221. (in

Chinese)

20. Montgomery, P.J. and T.B. Moodie (2003), "Generalization of a relaxation scheme for systems of forced nonlinear hyperbolic conservation laws with spatially dependent flux functions," *Studies in Applied Mathematics*, 110(1): 1-19.
21. O' Brien, J.S. (2003), *FLO-2D users manual*, FLO Engineering, Inc.
22. O' Brien, J.S., Julien, P.Y. and W.T. Fullerton (1993), "Two-dimensional water flood and mudflow simulation," *J. Hydr. Engrg.*, ASCE, 119(2): 244-261.
23. Peng, S.H. (2004), *The interactive mechanism of influence in main river morphology induced by hyperconcentrated tributary inflow*, Ph.D. thesis, National Chung-Hsing University, Taiwan. (in preparation)
24. Salmon, R. (2002), "Numerical solution of the two-layer shallow water equations with bottom topography," *Journal of Marine Research*, 60(4): 605-638.
25. Stoker, J.J. (1957), *Water waves*, Interscience.
26. Toro, E.F. (1999), *Riemann solvers and numerical methods for fluid dynamics: a practical introduction*, 2nd ed., Springer, Berlin.
27. Wang, Z.L. and H.T. Shen (1999), "Lagrangian simulation of one-dimensional dam-break flow," *J. Hydr. Engrg.*, ASCE, 125(11): 1217-1221.

Appendix A

Assuming that mud behaves as a Herschel and Bulkley fluid, its rheology is described by the relation

$$t = t_y + K\dot{g}^n, \tag{A.1}$$

whereby beyond a certain yield stress t_y the shear stress grows non-linearly with the strain rate $\dot{g} = \frac{du}{dy}$, with a corresponding dynamic viscosity K and the flow index n. The parameter K is also called consistency index which grows higher indicating the greater viscosity of fluid. The parameter n is also named as flow behavior index which represents the index of deviation from the Newtonian fluid. It will be the Bingham fluid when n = 1, and the Herschel and Bulkley fluid is similar to Bingham fluid, i.e. it will start to move when the shear stress of flow is greater than the yield stress.

For long waves, the vertical velocity and shear stress profiles adopt the structure shown on Fig. A.1. The flowing layer is subdivided into 1) an upper plug-flow region ($H < y < h_1$), moving rigidly at a velocity $u = u_p$, and 2) a lower shear-flow region, where u varies from zero to u_p as y goes from 0 to H. Balancing the slope-wise component of the weight, the shear stress t varies linearly with depth according to the relation

$$t(y) = t_0\left(1 - \frac{y}{h_1}\right), \tag{A.2}$$

where $t_0 = r_1 g h \sin q$ is the shear stress acting on the bed, r_1 is the density of the mud, g is the acceleration due to gravity, and $\sin q$ is the bed slope. In the plug-flow region, the depth of plug-flow d_0 is equal to (h_1 - H) when $t = t_y$ and $y = H$. Substituting for the known condition, we obtain

$$d_0 = \frac{t_y}{r_1 g \sin q}. \tag{A.3}$$

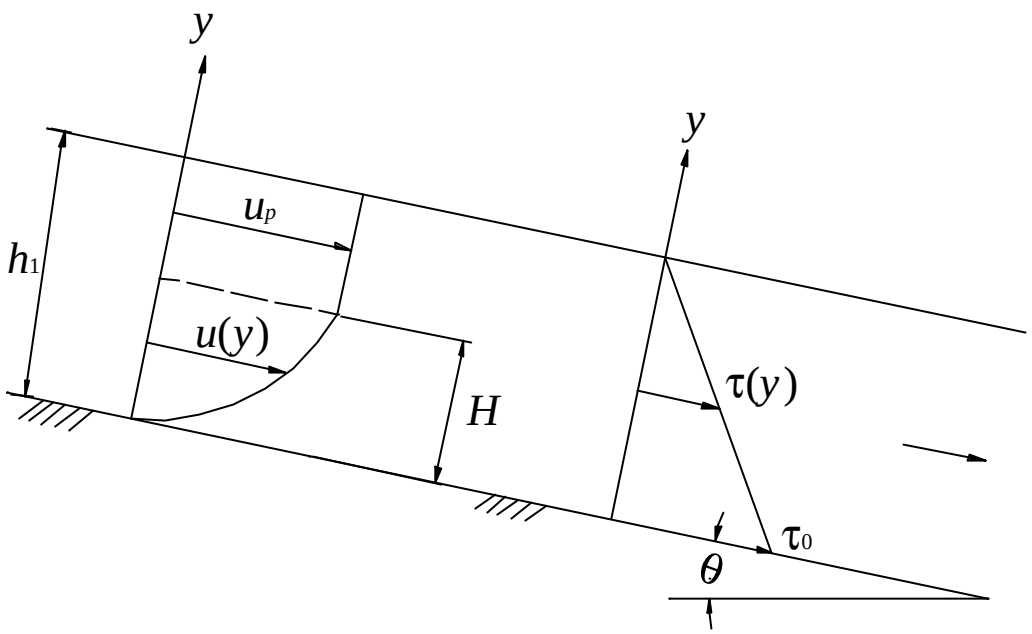

Figure A.1. Shear stress and velocity distribution.

In the shear-flow region, the velocity profile can be derived from integrating (A.1) as follows:

$$u(y) = \int \left(\frac{t - t_y}{K} \right)^{\frac{1}{n}} dy \qquad \text{for } 0 \le y \le H . \tag{A.4}$$

Substituting equations (A.2), (A.3) and boundary conditions: $y = 0$, $u = 0$ in (A.4)

$$u(y) = \frac{n}{n+1} \left(\frac{r_1 g H^{n+1} \sin q}{K} \right)^{\frac{1}{n}} \left[1 - \left(1 - \frac{y}{H} \right)^{\frac{n+1}{n}} \right] \qquad \text{for } 0 \le y \le H . \tag{A.5}$$

The velocity u_p of the rigid-like plug is obtained by substituting $y = H$ in (A.5):

$$u_p = \frac{n}{n+1} \left(\frac{r_1 g H^{n+1} \sin q}{K} \right)^{\frac{1}{n}} \qquad \text{for } H \le y \le h_1 . \tag{A.6}$$

The mean velocity u_1 can thus be retrieved from

$$u_1 = \frac{1}{h_1}\left[\int_0^H u(y)dy + \int_H^{h_1} u_p dy\right] = \frac{n}{n+1}\left(\frac{r_1 g H^{n+1}\sin q}{K}\right)^{\frac{1}{n}}\left(1 - \frac{n}{2n+1}\frac{H}{h_1}\right). \quad \text{(A.7)}$$

In the above results, the shear stress of bed t_0 can be obtained from the derivatives of (A.5) at $y = 0$ and substituting the stain rate of (A.1), i.e.

$$t_0 = t_y + K\left(\frac{du}{dy}\right)^n\Bigg|_{y=0}. \quad \text{(A.8)}$$

Substituting (A.7) for (A.8), the shear stress of bed can be expressed as

$$t_0 = t_y + K\left[\frac{1+\frac{1}{n}}{1-\frac{nH}{(2n+1)h_1}}\right]^n\left(\frac{u_1}{H}\right)^n, \quad \text{(A.9)}$$

which approximates the rheological relationship of Herschel and Bulkley model in the shallow flow conditions. The velocity profiles are shown in Fig. A.2 for different n values.

In the first, consider a hyperconcentrated flow, i.e. $t_y = 0$, $H = h_1$ and $n = 1$, so (A.9) can be reduced into a simpler form such as

$$t_0 = 3K\left(\frac{u_1}{h_1}\right). \quad \text{(A.10)}$$

In this case, the fluid usually obeys the law of Newtonian fluid and its viscosity will be a function of the concentration of sediment. Generally, the flow can be regarded as a hyperconcentrated flow while the concentration is less than 45 % (O' Brien, 2003).

Next, the Herschel and Bulkley fluid is identified with a Bingham fluid in which, beyond a certain yield stress t_y the shear stress grows linearly with the strain rate, with a corresponding dynamic viscosity K, when the flow index n is equal to unity. The shear stress t_0 acting on the bed can be obtained in the Bingham fluid model as

$$t_0 = t_y + K\frac{1}{\frac{1}{2} - \frac{H}{6h_1}}\left(\frac{u_1}{H}\right), \tag{A.11}$$

where the physical meaning of notations are the same as in the Herschel and Bulkley fluid model described above. It can simplify the calculation by choosing good fluid properties before numerical simulation in this model.

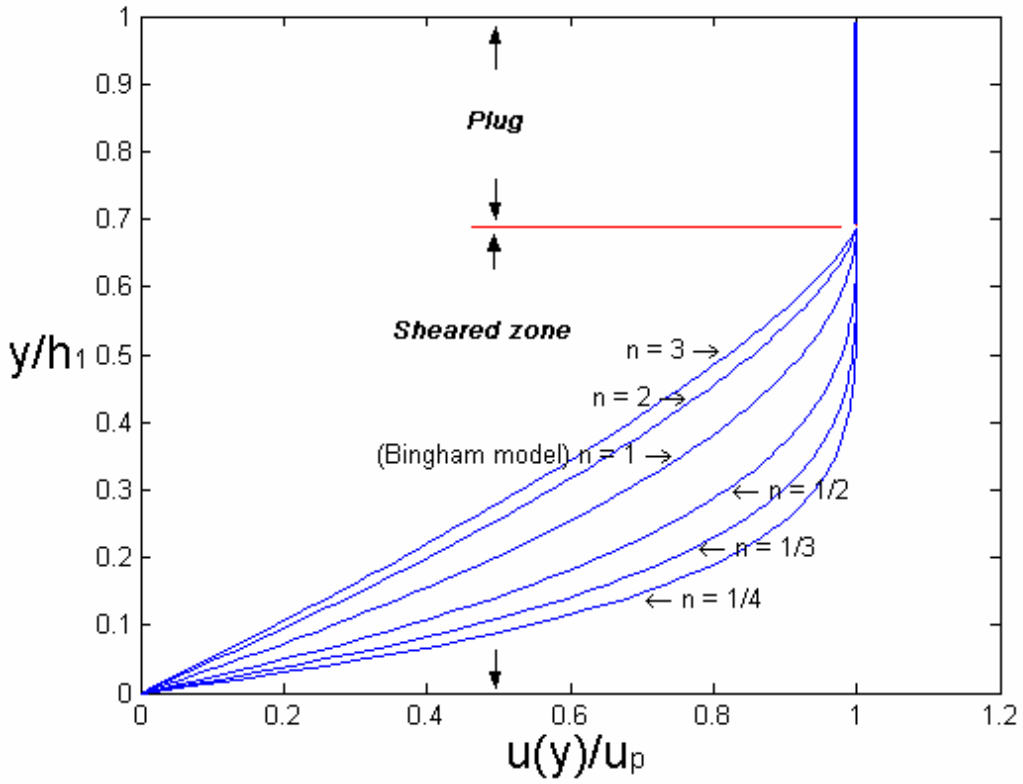

Figure A.2. Velocity distribution for a uniform flow of the Herschel & Bulkley model in different n values (where r_1 = 1650 kg/cm^3, t_y = 50 N/m^2, K = 20 N·s/m^2, sin$q$ = 0.01).